Liquid exfoliated $Co(OH)_2$ nanosheets as low-cost, yet high-performance, catalysts for the oxygen evolution reaction

David McAteer,[1#] Ian Godwin,[1#] Zheng Ling,[1] Andrew Harvey,[1] Lily He,[1] Conor S Boland,[1] Victor Vega-Mayoral,[1] Beata Szydlowska,[1] A.A. Rovetta,[2] Claudia Backes,[3] John B Boland,[1] Xin Chen,[2] Michael E.G. Lyons[2] and Jonathan N Coleman[1]*

[1]*School of Physics, CRANN & AMBER, Trinity College Dublin, Dublin 2, Ireland*

[2]*School of Chemistry, CRANN & AMBER, Trinity College Dublin, Dublin 2, Ireland*

[3]*Chair of Applied Physical Chemistry, Ruprecht-Karls University Heidelberg, Im Neuenheimer Feld 253, 69120 Heidelberg, Germany*

[#]These authors contributed equally

*colemaj@tcd.ie

ABSTRACT: Identifying cheap, yet effective, oxygen evolution catalysts is critical to the advancement of water splitting. Using liquid exfoliated $Co(OH)_2$ nanosheets as a model system, we developed a simple procedure to maximise the activity of any OER nano-catalyst. We first confirmed the nanosheet edges as the active areas by analysing the catalytic activity as a function of nanosheet size. This allowed us to select the smallest nanosheets (length~50 nm) as the best performing catalysts. While the number of active sites per unit electrode area can be increased via the electrode thickness, we found this to be impossible beyond ~10 μm due to mechanical instabilities. However, adding carbon nanotubes increased both toughness and conductivity significantly. These enhancements meant that composite electrodes consisting of small $Co(OH)_2$ nanosheets and 10wt% nanotubes could be made into free-standing films with thickness of up to 120 μm with no apparent electrical limitations. The presence of diffusion limitations resulted in an optimum electrode thickness of 70 μm, yielding a current density of 50 mA cm^{-2} at an overpotential of 235 mV, close to the state of the art in the field. Applying this procedure to a high performance catalyst such as $NiFeO_x$ should significantly surpass the state-of-the-art.

Keywords: nano-catalyst, layered material, exfoliation, oxygen evolution reaction, size-dependence

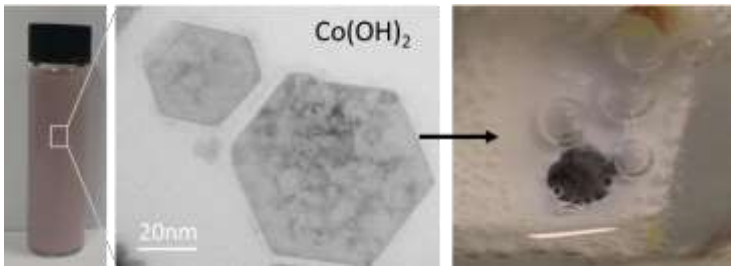

ToC fig

ToC text: Liquid exfoliation of $Co(OH)_2$ yields suspensions of nanosheets which are easily processed and so optimised for OER catalysis. This processability has allowed the variation of nanosheet size and the production of catalytic electrodes with controlled thickness as well as the addition of carbon nanotubes to enhance electrode conductivity and strength. This has resulted in an optimised electrode design with near record performance.

1. INTRODUCTION

Electrolysis is currently an important research area due to its potential to produce high purity hydrogen gas.[1] Due to the large associated overpotential, the most energetically inefficient part of the process is the oxygen evolution reaction (OER) at the anode.[2] To avoid expensive platinum group metals,[3] much work has focused on developing low-cost catalysts which generate reasonable oxygen production rates (*i.e.* current densities) at relatively low overpotentials.[4, 5] For alkaline electrolysis, oxides/hydroxides or chalcogenides of Ni, Co and/or Fe have proven to be the most effective catalysts.[6-10] Of these, 2-dimensional materials such as layered double hydroxides (LDH),[5, 6, 11] have attracted much focus, achieving current densities of 50 mA cm^{-2} at overpotentials as low as ~210 mV.[7] However, the best performing materials tend to require complex synthesis such that a system which combines high-performance with low cost has yet to be demonstrated.

In the literature, the usual approach is to produce new catalytic materials with superior intrinsic properties (e.g. increased turnover frequency) leading to better performance (often expressed via the overpotential required to achieve a current density of 10 mA cm^{-2}). This approach has led to the demonstration of some impressive materials.[7, 9, 12-14] However, it also has significant weakness in that many of the high-performance materials which have been demonstrated are complex structures[7, 9, 12, 13] (e.g. gelled FeCoW oxyhydroxide[9] or highly porous $Ni_xFe_{1-x}Se_2$ nanoplates[7]) which may be challenging to produce cheaply in large quantities.

We believe the traditional approach can be complemented by materials science methodologies to optimise the catalytic electrode, rather than the catalyst material. In OER, the O_2 production rate is represented by the current density, *J*, which must be maximised for a given overpotential. Because *J* is the product of an intrinsic activity and the electrode mass loading or thickness ($J = (I/M) \times M/A = (I/V) \times t$, where *I* is the current generated and *M*, *V*, *A* and *t* are the electrode mass, volume, area and thickness), both of these parameters must be simultaneously increased to achieve global performance maximisation. The traditional approach usually only addresses the intrinsic activity (*I/M* or *I/V*) by striving to produce new materials with larger turnover frequency or to increase density of active sites, for example by exfoliation.[6] Often, in the literature, such a novel catalyst is prepared and a single nominal mass deposited onto a support and tested for electrocatalytic performance.[11, 12, 14] Effectively, the electrode thickness is usually ignored with only a very few papers examining the dependence of activity on electrode thickness.[15-17] Where electrode thickness was varied, the maximum thickness was always less than a few microns, not enough to maximise OER performance.

There are a number of reasons why thickness dependent studies are not generally performed. By analogy with research on battery[18] or supercapacitor[19] electrodes and from the few available thickness-dependent OER studies,[16] it is known that, while performance increases at low thickness, it can saturate or decrease at higher thickness. There are a number of reasons for this, with the most well-known being mass-transport limitations; for thick electrodes, diffusion of ions from the bulk electrolyte can become rate limiting. However, it is perhaps less appreciated that thick electrodes can be electrically limited (the time to deliver charge to active sites can be rate limiting) or mechanically limited (poor mechanical robustness leads to electrode failure).[16, 19-21] In addition, it is not trivial to make arbitrarily thick electrodes from solution processed nanoparticles, due to mechanical instabilities above a critical thickness.[22] Because of these difficulties with thick electrodes, many researchers avoid them by using nickel foam supports[6, 12, 23, 24] to increase the catalyst mass per geometric area, while retaining low electrode thickness. However, using such foams may not be economically viable in real electrolysers.

We believe that the problems associated with producing high-performance, thick catalytic electrodes can be resolved using an holistic strategy which includes both catalyst optimisation and thickness maximisation. The aim of this paper is to develop a procedure which

can be applied to any solution-processable, nano-particulate OER catalyst to maximise its activity. While such a method should yield the best results when applied to a high-performance catalyst, if successful, it should also be able to dramatically improve the performance of a relatively poor catalytic material. This is important, as it could allow near state-of-the-art results to be obtained using a relatively cheap starting material.

Here we use layered cobalt hydroxide ($Co(OH)_2$, cost 41 cent g^{-1}) as a model OER catalyst to study electrode optimisation. To ensure scalability,[25] we use liquid phase exfoliation (LPE) to produce $Co(OH)_2$ nanosheets which were then selected by size.[26, 27] Analysing the dependence of OER activity on nanosheet size and electrode thickness confirmed nanosheet edges to be catalytically active and allowed us to select the smallest nanosheets as the best catalysts. Adding carbon nanotubes to the electrodes dramatically improved the mechanical, electrical and catalytic properties and allowed the production of free-standing films which were not mechanically or electrically limited. Using an optimised electrode thickness of 70 μm and tuning the electrolyte concentration and temperature, we were able to achieve current densities of 50 mA cm^{-2} at overpotentials as low as 235 mV, only 25 mV above the state-of-the-art (50 mA cm^{-2} @ 210 mV).[7]

2. RESULTS AND DISCUSSION

Liquid phase Exfoliation of $Co(OH)_2$

Cobalt hydroxide is a layered double hydroxide (figure 1A) with applications in a number of areas including electrocatalysis and electrodes for supercapacitors or batteries.[28, 29] Empirically, it has been shown that, like many other layered materials, $Co(OH)_2$ performance improves when exfoliated into thin 2D nanosheets.[28, 30, 31] However, in the past, LDH nanosheets have been produced by relatively complex methods such as hydrothermal synthesis coupled with exfoliation by ion exchange.[6, 7, 24, 32]

Here we take a simpler approach, using LPE as a top-down method to produce $Co(OH)_2$ nanosheets directly from the parent layered crystal. Liquid phase exfoliation is a simple, robust technique which can produce large volumes (>100s of litres)[25] of nanosheet dispersions in ambient conditions. Relatively high concentrations (~1 mg ml^{-1}) can be achieved with nanosheet dimensions of ~100s of nm across by ~nm thick.[26] This method is versatile,[33] having produced a range of 2D materials including graphene,[34] BN,[35] MoS_2,[36] SnO,[37] black

phosphorous,[38] franckeite,[39] layered silicates,[40] and particularly relevant, nanosheets of $Ni(OH)_2$.[27]

Here, we demonstrate that $Co(OH)_2$ nanosheets can be produced by this method. Layered $Co(OH)_2$, was purchased in powder form from Sigma Aldrich and washed to remove impurities.[27] The simplest, most reliable form of LPE involves high intensity ultrasonication of the layered powder in a water surfactant solution.[41] The ultrasound breaks up the layered crystals to give nanosheets which are rapidly coated with surfactant molecules, stabilising them against aggregation. Surfactant exfoliation has been applied to both uncharged (e.g. graphene and WS_2)[41] and charged (e.g. silicates)[40] layered materials and has been used to produce $Ni(OH)_2$ nanosheets.[27]

To exfoliate $Co(OH)_2$, the washed powder (C_i = 20 mg ml^{-1}) was added to an aqueous solution of the surfactant, sodium cholate, (V=80 ml, C_{SC} = 9 mg ml^{-1}) and sonicated (t =4 h) in a metal beaker using an ultrasonic tip (see Methods). The dispersion was then centrifuged (t_{cf} = 120 min at 1.5 krpm, 240 g) to remove non-exfoliated material. This set of conditions results in a stable dispersion (figure 1B) with the pale pink colour expected for β-$Co(OH)_2$,[42] which we refer to as the standard sample. Additional experiments (see figure S1) showed these parameters to be near-optimal. The success of the exfoliation procedure was confirmed by transmission electron microscopy (TEM) which showed the dispersion to contain large quantities of well-exfoliated, electron transparent nanosheets with well-defined edges as seen in figure 1C. Statistical analysis of TEM images shows the nanosheets in the standard sample to be quite small, with lateral sizes (length, L, defined as maximum dimension) between ~20 and ~300 nm ($\langle L \rangle$ = 88±5 nm, figure 1D). Not all nanosheets were perfectly hexagonal yielding a mean length/width aspect ratio of 1.3±0.1. AFM analysis (figure 1E) showed the nanosheet thickness (presented as number of monolayers per nanosheet, N) to vary between 2 and ~10 and gave an L-distribution similar to TEM ($\langle N \rangle$=6.2±0.2, also $\langle L \rangle$ = 94±4 nm).

One advantage of working with nanosheet dispersions is the ease with which they can be processed into structures such as films. We note that care was taken to heavily wash the films to remove any residual surfactant (see figures S5-6). Shown in figure 1F is a vacuum filtered film of $Co(OH)_2$ nanosheets (~0.1 mg.cm^{-2}) which clearly consists of a disordered, porous nanosheet network. The measured density of such films is ~2300 kg.m^{-3} implying a fractional pore volume of ~35%. This high porosity will allow electrolyte infiltration and makes such networks ideal for electrochemical applications.[43]

X-ray photo-electron spectroscopy (XPS) was used to confirm the chemical composition of the exfoliated nanosheets.[44] Shown in figure 1G-H are Co 2p and O 1s XPS core level spectra measured on both the washed powder and filtered films of exfoliated nanosheets. Fittings showed both the powder and the nanosheets to exist primarily of $Co(OH)_2$ with approximately 5% and 3% being contributed by CoOOH and CoO respectively. The corresponding O 1s core-level spectra show the expected $Co(OH)_2$ contribution at 531 eV (grey). There is also a broad component on the high binding energy shoulder (grey), which is most likely associated with impurities.

To test the electrocatalytic performance of our exfoliated $Co(OH)_2$ nanosheets, we measured linear sweep voltammograms (LSVs) for a 0.1 mg cm^{-2} film of standard sample nanosheets deposited on glassy carbon (GC) as shown in figure 1I (1 M NaOH). This curve shows the expected exponential increase and reaches a current density of 10 mA cm^{-2} at an overpotential of 440 mV. This performance is not exceptional: $Co(OH)_2$ electrocatalysts reach 10 mA cm^{-2} at overpotentials in the range 300 – 450 mV.[28, 30, 45] However, LPE-based samples have a significant advantage in that production and processing is very simple. This will facilitate electrode optimisation leading to significant improvements in the OER performance.

Optimisation of Catalytic Performance: Length Dependence and Nanosheet Edges

To maximise catalytic performance, it is necessary to identify the active sites for OER catalysis. Similar to hydrogen evolution electrocatalysis,[46, 47] nanosheet edges are often assumed to be active for OER catalysis.[5-7] While Chen and Selloni[48] used DFT to suggest edges to be the most likely active sites for $Co(OH)_2$, this has not been confirmed experimentally. In addition, Song et al[6] linked the improved activity of their exfoliated LDHs compared to bulk samples to the increased number of edge sites but highlighted the requirement for a rigorous study to prove this correlation. Here, we attempt to show categorically that the active sites for $Co(OH)_2$ OER catalysts lie on the nanosheet edges.

Recently we have shown that, for gas evolution reactions catalysed by nanosheets where the active sites are at the edges, the observed current density, *J*, is given by a specialised version of the Tafel equation[20, 47]

$$J = 2ne[R_0B]\times 10^{\eta/b}\times\left[\frac{(1+k)(1-P)}{\langle L\rangle d_0}\right]t \qquad (1a)$$

where η is the overpotential, b is the Tafel slope, n is the number of electrons supplied per gas molecule formed (here O_2 so n=4), R_0 is the zero-overpotential turnover frequency (per site), B is the number of catalytic active sites per unit nanosheet edge length, k is the nanosheet length/width aspect ratio, P is the electrode porosity, $\langle L \rangle$ is the mean nanosheet length, d_0 is the monolayer thickness and t is the electrode thickness. Here the product R_0B is the number of O_2 molecules produced per second per unit edge length (including edges associated with all individual layers stacked in few-layer nanosheets) at zero overpotential and can be thought of as a figure of merit for the catalytic activity of a nanosheet.

Clearly, this equation predicts that, if the edges are active, the current density at a given overpotential will scale inversely with $\langle L \rangle$. In addition, it predicts that the overpotential at a given current density, J, scales as

$$\eta_J = b \log \langle L \rangle + C(J) \qquad (1b)$$

where C is a combination of other parameters, including J. Thus, by analysing the dependence of catalytic performance on nanosheet length, one can determine whether or not edges are the active sites.

To perform such experiments, a stock dispersion produced by LPE was separated into 14 fractions containing different size nanosheets using liquid cascade centrifugation[26] (see methods). Flake lengths were determined using combined UV-vis extinction spectroscopy and statistical TEM analysis (see SI) yielding values of $\langle L \rangle$ between 36 and 184 nm. Typical TEM images of the smallest and largest fractions are shown in figure 2A-B. These size-selected dispersions were used to prepare porous films of stacked nanosheets of approximately equal masses of ~0.1 mg cm^{-2} and with electrode thicknesses, measured by profilometry, of ~420 nm. The densities of these films were typically 2330±400 $kg.m^{-3}$, leading to porosities of roughly 35±9%. A section of each film was then transferred onto glassy carbon electrodes for electrochemical testing (see Methods).

To test the electrocatalytic performance of such electrodes, LSVs (1 mV s^{-1}, 1 M NaOH) were performed in a three electrode cell. Typical curves are shown in figure 2C and clearly show improved catalytic performance as $\langle L \rangle$ is decreased. Ideally, one would fit the linear portion of the LSVs to the Tafel equation and extract the Tafel slope and the exchange current density. However, this procedure did not yield reliable values of either parameter due to the lack of a fully-developed linear region (see figure S8). As shown in the inset of figure 2C, curvature is observed at both low and high overpotential with detailed analysis showing no

region of linearity (see SI). We could only conclude that the apparent Tafel slope was ~60 mV dec^{-1} for all nanosheet lengths, consistent with literature reports.[6]

To properly analyse the data, careful choice of metrics is important. To apply quantitative analysis based on the Tafel equation (equations 1a-c), one must first identify regions of the Tafel plot which are as close to linearity as possible. As shown in figure S9, this was found to be the case for overpotentials close to 0.3 V and current densities in the region of 0.5 $mA.cm^{-2}$ for all nanosheet lengths. Based on this, for each nanosheet length, we extracted from the LSVs the overpotential at 0.5 $mA.cm^{-2}$ ($\eta_{0.5mA/cm2}$) and the current density at 0.3 V ($J_{0.3V}$) as metrics for catalytic performance. In addition, to provide continuity and allow comparison with the literature, we extracted data for the overpotential at 10 $mA.cm^{-2}$ ($\eta_{10mA/cm2}$). These parameters are plotted versus $\langle L \rangle$ in figures 2D-E and show a logarithmic increase in $\eta_{0.5mA/cm2}$ with $\langle L \rangle$ and a linear scaling of $J_{0.3V}$ with $1/\langle L \rangle$, exactly as predicted by equations 1b and 1a respectively. This agreement between experiment and theory is very strong evidence that the catalytically active sites do indeed reside on the edges of $Co(OH)_2$ nanosheets. Further analysis to rule out the possibility of basal plane activity can be found in the SI. Fitting the data in figure 2D to equation 1b yields an effective Tafel slope of b=69±13 mV dec^{-1}, in reasonable agreement with the LSVs.

The length-dependent data described above clearly shows the smallest nanosheets to be the best OER catalysts because of their high edge content. Thus, for the rest of this work, we will use a size selection scheme (see Methods) designed to give the smallest nanosheets which are attainable at a reasonable mass yield. We label this fraction s-$Co(OH)_2$, with AFM characterisation (figure 2F) showing it to contain nanosheets with $\langle N \rangle$=4.8±0.3 and $\langle L \rangle$=57±4 nm.

Optimisation of Catalytic Performance: Nanosheet Edges and Electrode Thickness

Optimising catalytic electrodes requires maximising the total number of active sites in a given area, which can be achieved by increasing electrode thickness or mass per unit area. This is illustrated by equation 1a which shows the current density to scale linearly with electrode thickness (t) and implies the overpotential at a given current density (J) to scale as

$$\eta_J = -b \log t + C'(J) \qquad (1c)$$

where C' is a combination of other parameters, including J.

To examine the thickness dependence, we used s-$Co(OH)_2$ nanosheets to produce a range of electrodes (on glassy carbon) with *M/A* ranging from 0.042 to 1.7 mg cm^{-2} ($0.22 \leq t \leq 8.3$ μm), a considerably broader range than tested previously in the literature.[6-8, 15, 23, 28, 49, 50] The average film density was found to be 2060±60 $kg.m^{-3}$ leading to an average porosity of 43±2% (see figure S7).

LSVs were obtained for each film thickness, with representative curves shown in figure 2G. As expected, we see a significant performance increase as the thickness is increased which we associate with the increase in the number of active sites. As before, the linear region was not extensive enough to generate reliable data beyond the fact that *b*~60 mV dec^{-1} for all electrodes (see figure S8).

Using the same procedure as before, we identified metrics which best represent the linear portion of the Tafel plot (see SI) as $\eta_{3mA/cm2}$ and $J_{0.3V}$. Along with $\eta_{10mA/cm2}$, these parameters are plotted versus film thickness in figures 2H-I. This data shows a logarithmic decrease of $\eta_{3mA/cm2}$ with *t* and a linear scaling of $J_{0.3V}$ with *t* exactly as predicted by equations 1c and 1a respectively. Fitting the data in figure 2H to equation 1c yields an effective Tafel slope of *b*=58±5 mV dec^{-1}, in good agreement with the LSV data. That the current density (i.e. the oxygen production rate) increases linearly with electrode thickness over the entire thickness range indicates that the entire electrode volume is active, even up to *t*~10 μm. This might appear surprising given the expected low conductivity of $Co(OH)_2$. However, recent work on $Co(OH)_2$ supercapacitor electrodes in our group has shown the out-of-plane conductivity to be as high as ~5×10^{-4} S/m, probably due to partial oxidation of the nanosheets.[21] This conductivity, although low, is enough to allow charge distribution throughout the film.

Edges are Active Sites Throughout the Film

It is clear that the outputs of fitting the *L*- and *t*-dependent data using the edge-active site model represented by equations 1 a-c are in good agreement. The obtained Tafel slopes (69±13 vs. 58±5 mV dec^{-1} respectively) agree within error and are in line with the values of ~60 mV.dec^{-1} implied by the LSVs and with literature values.[6] However, a better way to compare the *L*- and *t*-dependent data is to note that equation 1a predicts the ratio of $t^{-1}dJ_{0.3V}/d(1/L)|_{\text{constant t}}$ to $dJ_{0.3V}/dt|_{\text{constant L}}$ should equal the mean nanosheet length for the experiments performed while varying film thickness. Taking the ratio of experimental slopes and $\langle t \rangle$=417 nm gives a nanosheet length of 62 nm which can be compared with the value of $\langle L \rangle$=57 nm measured by AFM. This agreement is excellent and is very strong evidence that

the data is consistent with the edge-active site model represented by equations 1 a-c. This of course consistent with the idea that the active sites reside on the nanosheet edges.

Calculating the figure of merit, R_0B accurately is difficult due to the uncertainty in the Tafel slope. However, we found the data fits in figure 2H to give the lowest error: $R_0B \approx 685 \pm 100$ s^{-1} m^{-1}. Using the data in figure 2I, we can more accurately estimate the oxygen production rate at η=0.3 V ($R_\eta B = R_0 B \times 10^{\eta/b}$) as 108±25 molecules s^{-1} μm^{-1} of edge length.

It can be of interest to compare this value to typical calculated TOF of $Co(OH)_2$ in the literature to measure active site density. Although it should be noted that most TOF calculations for $Co(OH)_2$ are based on non-ideal assumptions about number of active sites (usually calculated from the voltammetric charge) and thus can generally be considered conservative estimates. Taking R_η = 0.09 s^{-1} (η=300mV) from reference[28] and comparing with the value of $R_\eta B$ quoted above, we can find a value for B = 1.2 nm^{-1} or in other words there is an active site every 0.83 nm along the nanosheet edge. Because, the characteristic in-plane separation of Co atoms in $Co(OH)_2$ is 0.27 nm, approximately 1 in every 3 Co edge atoms is active in our nanosheets. This may imply that Co atoms in certain edge structures are not active.

The observed linear scaling of $J_{0.3V}$ with t suggests that O_2 is being generated throughout the porous film even up to film thicknesses as high as 9 μm. This lack of current saturation at high electrode thickness is in contrast to most of the literature[6, 8, 51] and may be related to the relatively high porosity achieved here. In general, electrochemical systems such as electrocatalysts, battery or supercapacitor electrodes experience performance saturation at high electrode thickness due to diffusion or charge transport limitations or possibly a reduction in mechanical integrity.[19, 20, 52] Despite the linear scaling, this work is indeed limited by problems at high electrode thickness. We found t=9 μm to be the highest thickness where we could make $Co(OH)_2$ nanosheet films reliably without spontaneous cracking during film drying or transfer to GC. This is a manifestation of the so-called critical cracking thickness (CCT), which is the maximum achievable thickness of granular films before the onset of mechanical instabilities.[22] This is a significant issue as the only way to continue to improve performance of our electrodes is to further increase the thickness. What is required is a method to increase the CCT while at the same time removing the charge transport limitations which are expected for very thick electrodes.[53] Achieving this would leave only mass transport (diffusion) effects to limit the performance of very thick electrodes.

Optimisation of Catalytic Performance: Adding Carbon Nanotubes

Because the CCT scales with the fracture toughness of the film,[22] the simplest approach to increasing it is to improve the mechanical properties of the electrode material. Improvement in both mechanical and electrical properties of nanosheet networks can be achieved by incorporating carbon nanotubes.[52] Adding as little as 5wt% single walled nanotubes (SWNTs) to a network of MoS_2 nanosheets has been shown to improve both tensile toughness and electrical conductivity by ×100 and $\times 10^8$ respectively.[52] In electrochemical devices, improvements in performance have been observed when adding SWNTs to MoS_2 hydrogen evolution catalysts,[20] as well as battery[52] and supercapacitor[19, 21] electrodes. However, while nanotubes have been used as anchoring sites for catalytic particles in OER electrodes,[54] they have not been systematically used to control their mechanical or electrical properties. It is also worth noting that graphene has been used as anchoring sites for catalytic particles.[1] However, while graphene will certainly improve electrode conductivity, for geometrical reasons it is unlikely to enhance the mechanical properties as nanotubes do.[52]

To test the effect of SWNTs on s-$Co(OH)_2$ films, we prepared a range of SWNT/$Co(OH)_2$ composites films. For mechanical measurements, thick, free-standing composites were made while for electrical and electrochemical measurements, thinner films were prepared and transferred onto glass and GC respectively. The SWNT mass fraction, $M_f = M_{\mathrm{CNT}} / (M_{\mathrm{CNT}} + M_{\mathrm{Co(OH)2}})$ was varied between 0.01 – 20wt% while the active $Co(OH)_2$ mass was kept constant. Typically M_f was converted to volume fraction, $\phi = V_{\mathrm{NT}} / (V_{\mathrm{NT}} + V_{\mathrm{Co(OH)2}}) = M_f \, \rho_{film} / \rho_{NT}$ for quantitative analysis.

To determine the effect of adding SWNTs to the mechanical properties of $Co(OH)_2$-based films, we performed tensile stress-strain measurements on thick, free-standing composite films (~4 mg cm^{-2}, t=18–28 μm, see Methods). Shown in figure 3A are typical stress-strain curves for composites with different SWNT content (see SI for all data). Clearly the addition of nanotubes drastically improves the stiffness, strength and toughness (area under stress-strain curve) of the electrodes. Previously, the toughness, which is a measure of the volumetric fracture energy, has been linked with the cycling stability of battery electrodes.[52] The toughness, T, is plotted in figure 3B versus SWNT volume fraction and shows a 1000-fold improvement, characterised by a sharp increase at ϕ~5vol%. It has been suggested[52] that such an increase coincides with the formation of a fully-formed nanotube network with the toughness increase subsequently described by percolation theory: $T - T_0 \propto (\phi - \phi_{c,m})^{n_m}$, where T_0 is the toughness of a nanosheet-only electrode. Fitting gives the mechanical percolation

threshold and exponent to be $\phi_{c,m}$=4.8vol% and n_m=0.6 respectively, similar to previous reports.[52] We note that the reinforcement mechanism is in-part associated with the fact that cracking is suppressed by bridging with nanotubes (figure 3B inset).

While this significant toughness enhancement would be expected to increase the CCT and so stabilise thick composite films, adding nanotubes yields further benefits. As described above, thick electrodes can become limited by slow charge transport from the current collector to active sites. The out-of-plane conductivity of LPE $Co(OH)_2$ electrodes (in 1M NaOH) has recently been reported to be ~5×10^{-4} S/m.[21] While this value is not extremely low, studies on $Co(OH)_2$-based supercapacitors have shown nanotube addition to yield significant performance enhancements.[21] Here we found that adding SWNTs significantly increases the dry (no electrolyte) in-plane electrical conductivity, σ, as shown in figure 3C for s-$Co(OH)_2$/SWNT films (0.9 mg cm^{-2}). The conductivity increased by $\times10^{10}$, with a sharp increase at a nanotube volume fraction of ~0.1vol%. Again, this can be described by percolation theory:[55] $\sigma \propto (\phi - \phi_{c,e})^{n_e}$, with fitting giving the electrical percolation threshold and exponent to be $\phi_{c,e}$=0.15vol% and n_m=2.2, also in line with previous 1D:2D composites.[19, 20, 52] However, we note that in catalytic electrodes, the technologically relevant parameter is the wet (in the presence of electrolyte) out-of-plane conductivity. Based on previous results,[21] we would expect this increase in in-plane conductivity to translate to a roughly ×100 increase in wet out-of-plane conductivity for the 10 wt% composite relative to the pure $Co(OH)_2$ electrode (in the presence of electrolyte).

Because of the conductivity increase with nanotube addition, it is likely that the catalytic performance also improves due to more efficient charge distribution. To examine this, we made a series of composite films from 0 wt% to 10 wt% (0.9 mg cm^{-2} s-$Co(OH)_2$) and performed linear voltage sweep measurements as shown in figure 3D. The effect of the SWNTs is immediately apparent with higher current densities achieved at lower OER onset potentials.

Again, as metrics, we plot $\eta_{10mA/cm2}$ and $J_{0.3V}$ as a function of CNT volume fraction in figures 3E-F respectively. In both cases we found unambiguous improvements with $\eta_{10mA/cm2}$ falling from ~335 to ~295 mV and $J_{0.3V}$ increasing from 3.1 to 14 mA cm^{-2}, as the SWNT content increased. These improvements are significant and highlight the utility of incorporating nanotubes in OER catalytic electrodes.

Production of High Performance Free-Standing Composite Electrodes

Although the increase in mechanical properties associated with the addition of nanotubes allows the production of composite films with thickness considerably greater than 9 μm, we found it impossible to transfer films >14 μm thick to the GC support due to adhesion problems (see figure S16C). To avoid this issue, we decided to study thick free-standing films as OER catalysts. A series of free-standing films were prepared using s-$Co(OH)_2$ mixed with 10wt% SWNTs, with thicknesses in the range 19–120 μm (3–13 mg cm^{-2}). An example of such a film is shown in figure 4A-C with the SEM image in figure 4D showing the SWNTs to be evenly dispersed throughout the electrode.

Shown in figure 4E are LSVs for a number of free-standing s-$Co(OH)_2$/SWNT composite electrodes of different thicknesses. Note that unless otherwise stated, all potentials quoted for free-standing films have not been iR corrected. Due to the relatively large mass of $Co(OH)_2$ used in the free-standing films, double layer capacitive currents contributed non-negligibly, introducing errors into measurements involving small currents (see figure S18). As a result, for the free-standing films, we use the overpotential at 50 mA cm^{-2} (i.e. $\eta_{50mA/cm2}$ rather than $\eta_{10mA/cm2}$) as a performance metric.

For free-standing electrodes, the current density tended to increase sub-linearly with η at high overpotential due to diffusion limitations. As shown in figure 4F, $\eta_{50mA/cm2}$ displays a well-defined minimum of around 420 mV, for a free-standing film thickness of between 50-70 μm. The increase in $\eta_{50mA/cm2}$ above t~70 μm is most likely related to electrolyte diffusion limitations and gas shielding effects. At higher thicknesses, the benefits associated with the addition of extra mass are countered by the limiting effects of diffusion of electrolyte into the internal surface which also increase with increasing film thickness. In addition, gas generated throughout the FS film can block fresh electrolyte from reaching active sites as it is escapes from the porous film. This shielding effect grows with film thickness and at thickness greater than 70 μm the effect becomes large enough to reduce catalyst activity.

For all subsequent experiments, we used an optimised 70 μm thick composite electrode containing s-$Co(OH)_2$ mixed with 10wt% SWNTs. Films prepared using this method were found to be extremely robust under vigorous oxygen evolution. This is illustrated in figure 4G which shows that, for an optimised composite electrode, currents of >1 A.cm^{-2} can be achieved while the overpotential required to generate a fixed high current density of 200 mA cm^{-2} remained relatively constant over a period of 24 hours (we use a different metric here because

of higher currents being possible with the optimised electrode). It should be noted that this current density is 20 times higher than the 10 mA cm^{-2} commonly used in the stability testing of OER catalysts.[56]

Although electrolytes with concentrations of 0.1-1 M KOH or NaOH are widely used to characterise potential OER catalysts in the literature[57], in industrial alkaline electrolysers it is common to use 30wt% or ~7 M KOH. Such high concentrations yield higher currents at a given overpotential[58] and result in lower Ohmic solution resistances. With this in mind, for the optimised composite electrode, we measured the overpotential required to achieve 50 mA cm^{-2} for a range of OH^- concentrations. As shown in figure 4H, we found $\eta_{50mA/cm2}$ to fall by ~160 mV when increasing the concentration from 0.5 M to 5 M NaOH. Increasing the electrolyte concentration beyond this was shown to give no further decrease in overpotential.

Another parameter rarely examined or varied in the benchmarking of OER catalysts is the electrolyte temperature. While the bulk of OER data in the literature corresponds to room temperature (generally between 20-25°C)[59], we believe a temperature study is useful because, industrial alkaline electrolysers operate at elevated temperatures of at least 80°C.[60] With this in mind we varied the temperature (electrolyte concentration 5 M NaOH), as shown in figure 4I from 20-50°C and observed a 60 mV decrease in overpotentials required to achieve current densities of 50 and 100 mA cm^{-2}, reaching a global low of 236 mV and 268 mV respectively (iR corrected). This drop in overpotential at a fixed current with increasing temperature is consistent with the work of Miles and co-workers.[61] It was not possible to increase the temperature further as the reference electrode used was not rated for higher temperatures. It is worth nothing that even without these temperature and electrolyte optimisations, the activity of our free-standing electrodes far exceed comparable free-standing systems published recently in the literature.[62]

3. CONCLUSIONS

In this work we have demonstrated that low-cost $Co(OH)_2$ crystals can be exfoliated in surfactant solutions to give relatively thin $Co(OH)_2$ nanosheets. Thin films of these nanosheets act as average OER electrocatalysts, requiring 440 mV to generate 10 mA cm^{-2}. However, the advantage of liquid phase exfoliation is that it gives large quantities of nanosheets in a very processable form. This allowed us to perform multiple enhancements, perfecting the nanosheet size, improving the electrical and mechanical properties by adding nanotubes as well as

optimising the electrode thickness, the electrolyte concentration and the electrolyser temperature. Taken together, these improvements yield a composite electrode which can yield a current density of 50 mA cm^{-2} at an overpotential of 236 mV under realistic conditions.

In order to properly benchmark these optimisations and to put them into perspective, we have compared our results to the current state-of-the-art in OER catalysts. We have attempted to include a fair representation of the most active $Co(OH)_2$-based and other state-of-the-art materials tested at elevated temperatures and a higher base concentrations. These are quantified via the lowest reliable values of the overpotential required to generate 50 mA cm^{-2} we could find in the literature with the state-of-the-art being 211 mV.[7] The comparison is shown pictorially in figure 4K with our lowest $\eta_{50mA/cm2}$ obtained in this work given by the black dashed line. It is clear that our best result is a mere 25 mV off the state-of-the-art. We emphasise that our result utilised a cheap starting material coupled with a scalable processing procedure. By contrast, the state-of-the-art employs a more complex NiFeSe material, synthesized on Ni foam.[7] These methods are not practically scalable as they often require several high temperature steps in their synthesis, combined with hazardous starting materials such as hydrazine and DMF. In addition, our result relied on the combination of an average material coupled with a processing-based optimisation protocol. We believe that combining our optimisation protocol with a more active material could yield a catalyst which far exceeds the current state-of-the-art.

4. Methods

Materials

Cobalt hydroxide powder (>95% item no. 342440) and sodium cholate (SC, item no. C1254) were purchased from Sigma Aldrich. Single-walled carbon nanotubes (SWNTs) were obtained from Hanwah Nanotech CO., Ltd and Tubal™. De-ionized water was prepared in house.

Preparation of $Co(OH)_2$ nanosheets.

Cobalt hydroxide ($Co(OH)_2$) powder was pre-treated by sonication using a solid flathead sonic tip (probe diameter 13 mm, Sonics VCX-750 processor) in 80 mL deionised water in a metal cup for 2h. The dispersion was then centrifuged (Hettich Mikro 220R) at 4.5 krpm (2150*g*) for 1 h and the supernatant decanted, with the sediment being retained and dried at 60 ^oC. The pre-treated $Co(OH)_2$ was sonicated in surfactant and de-ionized water solution using a solid flat head tip at 60% amplitude with a 6 s on 2 s off pulse rate in an 80 ml metal cup. Ice cooling

was used to prevent heating caused by the sonic tip. Once sonicated, the dispersion was centrifuged with a fixed-angle rotor 1060 (N.B.: for this centrifuge, rpm are related to *g*-force *via* RCF = $106.4f^2$, where *f* is the rotation rate in krpm.) The top 60% was taken from the centrifuged sample (supernatant) for analysis and the sediment was discarded. After a surfactant concentration and initial $Co(OH)_2$ concentration study, the final optimised exfoliation was performed as follows: 20 mg/mL of $Co(OH)_2$ were sonicated for 4 h in 9 $mg.mL^{-1}$ of SC and then centrifuged for 120 min at 1.5 krpm (240*g*) to produce a standard $Co(OH)_2$ sample with average flake length, $\langle L \rangle$ = 90 nm.

Size Selection

We used liquid cascade centrifugation with subsequently increasing rotation speeds as previously reported.[26] 80 mL of exfoliated $Co(OH)_2$ dispersion was centrifuged at 0.5 krpm (27g) for 60 min. The sediment was discarded and the supernatant was centrifuged at 1 krpm (100g) for 60 min. The sediment after this centrifugation step was redispersed in fresh surfactant solution (C_{SC} = 9 g L^{-1}, 25 mL) for 5 min by bath sonication producing the largest size. The supernatant after the 1 krpm centrifugation step was centrifuged at 1.5 krpm (240g) for 60 min, producing the second largest size in the redispersed sediment. These steps were repeated in further increments of 2 krpm (425g), 2.5 krpm (665g), and 3 krpm (950g), thus producing additional sizes. The three smallest sizes were combined to make the s-$Co(OH)_2$ dispersion, with $\langle L \rangle$ = 50 nm, as a compromise between nanosheet size and produced mass. The yield of s-$Co(OH)_2$ nanosheets was ~ 3.5%. All $Co(OH)_2$ dispersion concentrations were found by vacuum filtering known volumes onto a Whatman® Anodisc inorganic filter membrane of a known weight, removing surfactant by filtering through 200 mL of deionized water, and left to dry. Once dry, the membrane was weighed and $Co(OH)_2$ dispersion concentration calculated. Nanosheet dimensions were measured using both spectroscopic and TEM analysis.

Characterization and Equipment.

Optical absorption and extinction measurements were performed in a 4 mm path length cuvette using a PerkinElmer Lambda 650 spectrometer with an integrating sphere attachment.

Low-resolution bright field transmission electron microscopy (TEM) imaging was performed using a JEOL 2100, operated at 200 kV. Holey carbon grids (400 mesh) were purchased from Agar Scientific and prepared by diluting a dispersion to a low concentration and drop casting

onto a grid placed on a filter membrane to wick away excess solvent. Statistical analysis was performed of the flake dimensions by measuring the longest axis of the nanosheet and assigning it as "length", L.

XPS spectra were taken using monochromated Al Kα X-rays from an Omicron XM1000 MkII X-ray source and an Omicron EA125 energy analyser. The analyser pass energies were 15 eV for the core-level spectra and 100 eV for the survey spectra. An electron Omicron CN10 flood gun was used for charge compensation in both cases and the binding energy scale was referenced to the adventitious carbon 1s core-level at 284.8 eV. After subtraction of a Shirley background, the core-level spectra were fitted with Gaussian-Lorentzian line shapes using the software CasaXPS.

Scanning electron microscopy (SEM) images were obtained using a ZEISS Ultra Plus (Carl Zeiss Group), 2 kV accelerating voltage, 30 μm aperture, and a working distance of approximately 1−2 mm.

See Supporting Information for more details on dispersion characterisation including Raman spectroscopy.

Preparation of SWNT Dispersions.

A 1 mg mL^{-1} dispersion of single-walled carbon nanotubes (SWNTs) was made by adding SWNT powder (Hanwah Nanotech CO., Ltd) to a stock solution of SC (10 mg mL^{-1} in deionized water), thus the resulting SWNT/SC mass ratio was 1:10. The dispersion was divided onto separate vials of 8 mL each and received 5 min high power tip sonication using a tapered microtip at 25% amplitude, pulse rate 2 s on 2 s off, then 30 min of bath sonication (Branson 1510-MT sonic bath, 20 kHz), followed by another 5 min tip sonication. The resulting dispersions were then centrifuged for 90 min at 5500 rpm and the supernatant of each was retrieved. The concentration of the SWNT dispersion was found by measuring the absorption at 660 nm using a Varian Cary 6000i. From the Beer-Lambert relation: $C = A/\varepsilon l$, the dispersion concentration, C, was found using the extinction coefficient of SWNT, 3389 mL mg^{-1} m^{-1} and cell length l = 1 cm. Typically SWNT concentration was between 0.5 – 0.4 mg mL^{-1}.

Film Formation and Device Preparation.

Dispersions of $Co(OH)_2$ in SC of a known concentration and volume were vacuum filtered through porous mixed cellulose ester filter membranes (MF-Milipore membrane, hydrophilic, 0.025 μm pore size, 47 mm diameter) resulting in spatially uniform films in a range of well-defined mass/areas (M/A). This method has the advantage of being able to control the deposited mass, and thus film thickness relatively accurately. The porous network type morphology of the resulting films is useful for applications in electrocatalysis, as it enables the free flow of electrolyte to the internal surface of the film.

Composite films of $Co(OH)_2$/SWNTs were made by first mixing a desired amount of the SWNT dispersion, based on the mass ratio needed, with the dispersion of $Co(OH)_2$ and bath sonicating for 30 mins until the two dispersions were well mixed. Films were then made using vacuum filtration.

Films were 'washed' to remove remaining surfactant by filtering 300 mL deionized water through the porous $Co(OH)_2$ or $Co(OH)_2$/SWNT network (see SI figure S5,6). The resulting films (diameter 36 mm) were then left dry overnight.

Once dry, the films were cut to desired dimensions and transferred onto glassy carbon (GC, CH Instruments, Inc) electrodes for electrochemical testing, glass substrates for profilometry thickness measurements and electrical measurements, and ITO glass for SEM imaging. The cellulose membrane was removed by applying pressure to the film onto a substrate, wetting it with acetone vapour, and then subjecting it to a series of acetone baths. The acetone dissolves the cellulose membrane, leaving behind the film on the substrate surface. To help with adhesion and stability during the gas bubbling Nafion (Nafion® 117 solution, Sigam-Aldrich) was added to all films transferred onto GC electrodes. A 5% Nafion solution was prepared in isopropyl alcohol (IPA) and 10 mL was dropcast onto the $Co(OH)_2$ films and allowed to dry in air.

Free-standing films were produced by first mixing the required amounts of $Co(OH)_2$ and SWNT dispersions (for mechanical testing, TUBAL™ SWNTs were used instead as they were available in larger quantities at a much lower cost and their higher impurity content should not hinder the mechanical analysis) and bath sonicating for 1 hr. The dispersions were then filtered through a PETE (Sterlitech) membrane. Making composite films, it was found to give better results filtering smaller volumes (~ 5 mL), thus for the free-standing films where larger volume are concerned, dispersions were filtered 5 mL at a time, adding the next 5 mL when the previous was settled on the surface. This resulted in a more even distribution of SWNTs throughout the $Co(OH)_2$ matrix. The films were then washed with 300 mL of deionized water and left to dry overnight. Once dry, the thick film could be peeled off the PETE membrane to give a free-standing film.

The free standing films were then mounted onto a stainless steel support and sandwiched between two PTFE sheets. The freestanding film has an exposed surface area of approximately 0.1 cm^2. An inert epoxy (Araldite®) was used to ensure complete isolation of the support from the electrolyte.

Electrode Characterization

Film thickness was measured using a Dektak 6M profilometer from Veeco Instruments. Step height profiles were taken at five different locations to get an average film thickness. Electrical conductivity measurements were taken with a Keithley 2400 source meter (Keithley Instruments, Inc.) using a four-probe technique. Silver wire contacts were painted on the film using Agar Scientific silver paint, and electrode spacing was recorded using ImageJ software. SWNT mass fraction, $M_f = M_{\mathrm{NT}} / (M_{\mathrm{NT}} + M_{Co(OH)2})$ was converted to volume fraction, $\phi = V_{\mathrm{NT}} / (V_{\mathrm{NT}} + V_{Co(OH)2}) = M_f \, \rho_{film} / \rho_{NT}$, where V_{NT} is the volume occupied by nanotubes, and ρ_{film} and ρ_{NT} are the densities of the film and the nanotubes, respectively (ρ_{NT} = 1500 kg/m^3). See Supporting Information for more details on electrode characterisation.

Electrochemical Measurements

All experiments were conducted in a conventional three electrode cell at a constant temperature of 20°C unless otherwise stated. For all the transferred films, a glassy carbon electrode (CH Instruments, CHI104) was used as a working electrode with a diameter of 3 mm. Prior to use, the glassy carbon electrode was polished with 0.3 μm alumina powder and triply rinsed with Millipore water (resistivity > 15 MΩ cm^{-1}) until a mirror finish was achieved. A spiral platinum rod was employed as the counter electrode and a mercury-mercuric oxide (Hg/HgO) reference electrode with a 1 M NaOH filling solution (CH Instruments, CHI 152) was utilised as the reference standard. All potentials quoted are with respect to the reversible hydrogen electrode (RHE), therefore it was necessary to convert the measured potentials to this. The equilibrium potential of the cell $Pt/H_2/OH^-/HgO/Hg$ is 0.926 V at 298 K. Since the equilibrium oxygen electrode potential is 1.229 V *vs*. RHE, it follows that the corresponding value is 0.303 V vs. Hg/HgO in the same solution. Hence $E_{Hg/HgO} = E_{RHE} - 0.926$ V. It is common practice in the literature on the OER to express potential in terms of the oxygen evolution overpotential, η, when the reference electrode is a Hg/HgO electrode in the same solution as the working anode. The overpotential therefore is related to E_{meas} measured on the Hg/HgO scale as follows: $E = E_{meas} - 0.303$ V (at T = 298 K).

Aqueous 1 M NaOH was used as the electrolyte unless clearly indicated otherwise. This solution was prepared from sodium hydroxide pellets (Sigma-Aldrich, minimum 99% purity). The electrochemical measurements were performed on a Gamry model 600 potentiostat/galvanostat. Linear sweep measurements were carried out at 1 mV s^{-1}. Where applicable the solution resistance was corrected using electrochemical impedance spectroscopy taking the resistance at the high frequency (>0.1 MHz) intercept of the Bode plot.

Acknowledgements

This work was predominantly funded by Science Foundation Ireland (11/PI/1087) as well as the European Union Seventh Framework Programme under grant agreement n°604391 Graphene Flagship and the Science Foundation Ireland (SFI) funded centre AMBER (SFI/12/RC/2278**).**

Figures

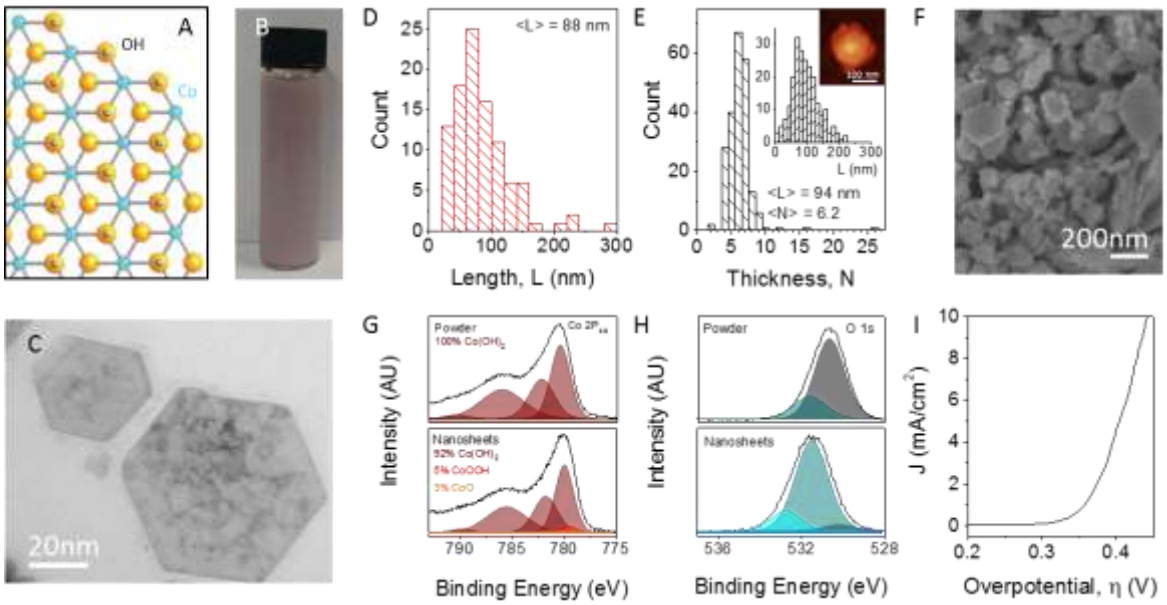

Figure 1: Exfoliation of $Co(OH)_2$ into nanosheets. (A) Structure of cobalt hydroxide, $Co(OH)_2$. Blue, Co; yellow, O; silver, H. (B) Photograph of typical $Co(OH)_2$ dispersion in surfactant solution (concentration of $Co(OH)_2$ was 7 mg mL^{-1}). (C) Representative low resolution TEM image of exfoliated $Co(OH)_2$ nanosheets. (D) Nanosheet length distribution as measured by TEM. (E) Nanosheet thickness (layer number) distributions as measured by AFM with length distribution and sample image shown in the inset. (F) SEM image of a vacuum filtered film of $Co(OH)_2$ nanosheets. (G) Co $2P_{3/2}$ XPS spectra of $Co(OH)_2$ pretreated bulk powder (top) and a film of reaggregated nanosheets (bottom). (H) O 1s core level spectra of pretreated powder (top) and film of reaggreagated nanosheets (bottom). (I) Polarisation curve for an electrode consisting of vacuum filtered $Co(OH)_2$ nanosheets on a glassy carbon electrode (1 M NaOH, scan rate 1 mV s^{-1}).

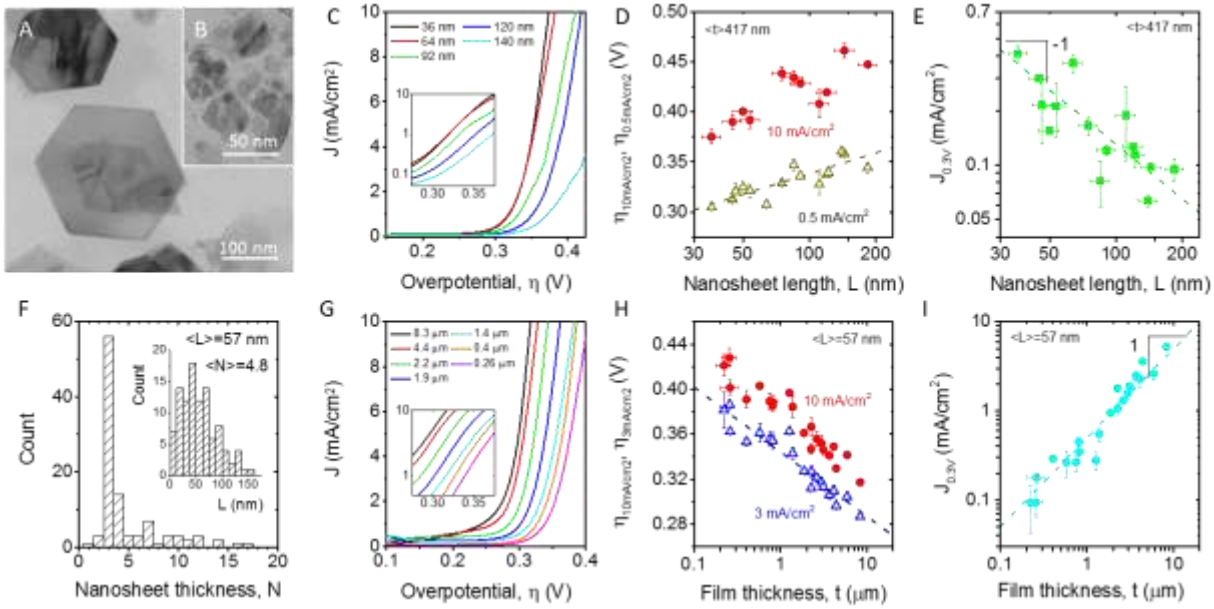

Figure 2: Nanosheet length- and electrode thickness-dependence. (A-B) Representative TEM images of nanosheets from the largest (A) and smallest (B) fractions. (C) Linear sweep voltammograms for $Co(OH)_2$ electrodes with a fixed thickness of ~0.45 μm (0.1 mg cm^{-2}) for a range of nanosheet lengths (1 M NaOH). Inset: corresponding Tafel plots. (D-E) Overpotential, measured at current densities of 10 and 0.5 mA cm^{-2}, (D) and current density, measured at η=0.3 V, (E), both plotted versus mean nanosheet length (on logarithmic scale). (F) AFM thickness distribution for s-$Co(OH)_2$ nanosheets. Inset: Corresponding length distribution. (G) Linear sweep voltammograms for electrodes of various thicknesses fabricated from s-$Co(OH)_2$ (1M NaOH). Inset: corresponding Tafel plots. (H-I) Overpotential, measured at current densities of 10 and 3 mA cm^{-2}, (H) and current density, measured at η=0.3 V, (I), both plotted versus film thickness. In (D) and (H), only the data measured at lower currents are fitted to equations 1 b and c as the currents used represent the portions of the Tafel plots most closely approximating linearity.

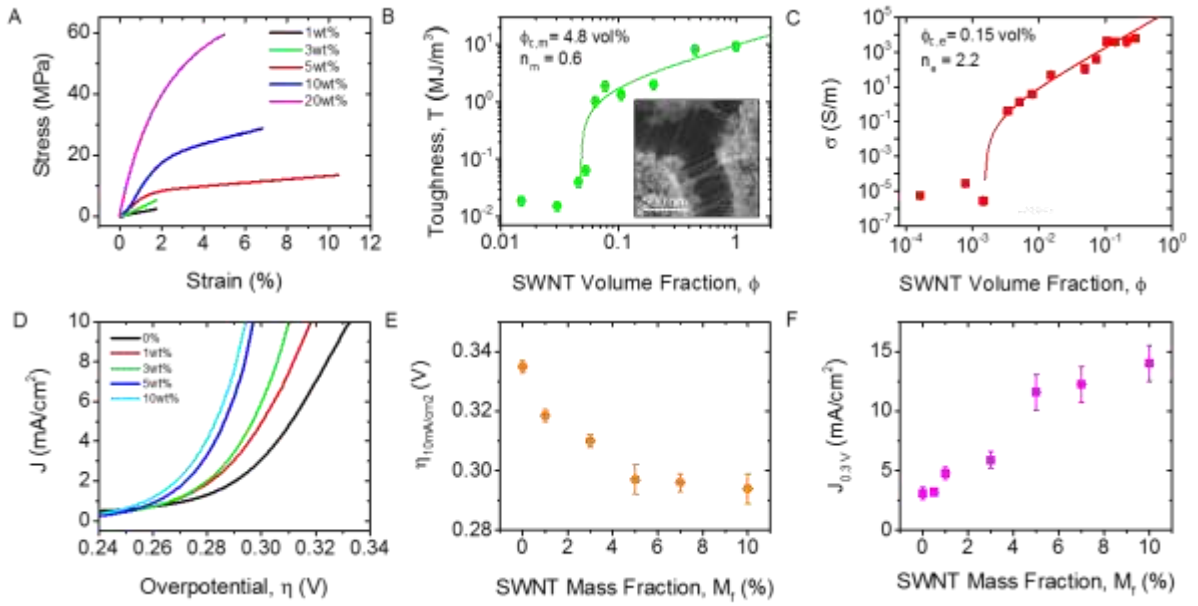

Figure 3: $Co(OH)_2$-SWNT composite OER catalysts. (A) Stress strain curves for a subset of composites. (B) Mechanical toughness (volumetric work to failure) as a function of volume fraction, ϕ, for free-standing composites of 4 mg cm^{-2} $Co(OH)_2$. Toughness is shown to scale with ϕ as per percolation theory. Inset: SEM image of $Co(OH)_2$/SWNT composite film with 1 wt% loading of SWNT, showing effective bridging of cracks by nanotubes. (C) In-plane electrical conductivity plotted against volume fraction of carbon nanotubes (SWNTs) in composite films of thickness 3.5–5.3 μm (~0.9 $mgcm^{-2}$ $Co(OH)_2$). Electrical conductivity is shown to fit to percolation theory. (D) Linear sweep voltammograms for composite electrodes with a fixed $Co(OH)_2$ loading of 0.9 mg cm^{-2} for a range of nanotube contents. (E) Overpotential required to produce 10 mA cm^{-2} and (F) current density at overpotential of 0.3 V, both plotted as a function of SWNT volume fraction. All figures pertain to s-$Co(OH)_2$ using 1 M NaOH as an electrolyte where applicable.

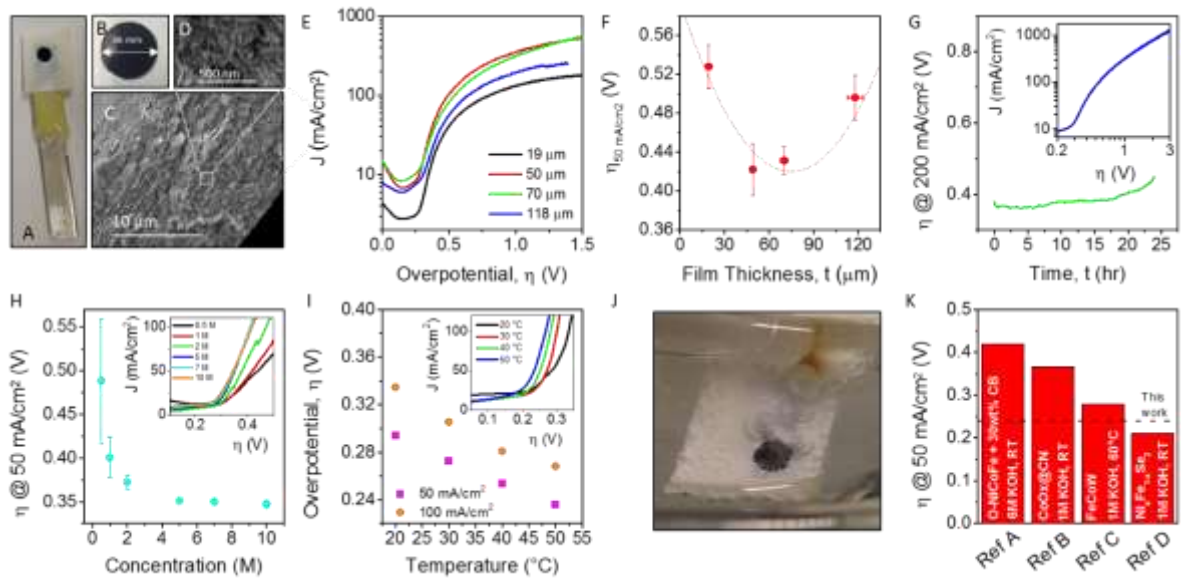

Figure 4: Free-standing composite catalytic electrodes. (A) Mounted free-standing composite electrode (exposed area of 0.1 cm^2) fabricated from free-standing composite film (B). (C-D) Cross-sectional SEM of composite film with protruding nanotubes shown in magnified region (D). (E) Representative linear sweep voltammograms as a function of film thickness in 1 M NaOH. (F) OER overpotential (50 mA cm^{-2}) vs. film thickness. The line is a guide to the eye. (G) Overpotential at 200 mA cm^{-2} vs. time for a 70 µm, 10wt% SWNT, s-$Co(OH)_2$ free-standing film. Inset: Corresponding linear sweep voltammogram showing capability of free-standing films to achieve high currents. (H) Overpotential at 50 mA cm^{-2} vs. electrolyte (NaOH) concentration. Inset: corresponding linear sweep voltammograms. (I) Overpotential at 50 and 100 mA cm^{-2} as a function of electrolyte temperature (inset: corresponding linear voltage sweeps) measured in 5 M NaOH electrolyte. (J) Photograph of a 70 µm free-standing film mounted electrode showing vigorous gas evolution. (K) Comparison of lowest overpotential at 50 mA cm^{-2} obtained in this work to the state-of-the-art materials in the literature. All figures pertain to a free-standing s-$Co(OH)_2$ with 10 wt% carbon nanotubes. Ref A = [49], Ref B = [8], Ref C = [9], Ref D = [7].

References

[1] Y. Liang, Y. Li, H. Wang, J. Zhou, J. Wang, T. Regier, H. Dai, *Nat. Mater.*, **2011**, *10*, 780.
[2] X. Long, J. Li, S. Xiao, K. Yan, Z. Wang, H. Chen, S. Yang, *Angew. Chem., Int. Ed. Engl.*, **2014**, *126*, 7714.
[3] J. Zhang, Z. Zhao, Z. Xia, L. Dai, *Nat. Nanotechnol.*, **2015**, *10*, 444.
[4] T. Y. Ma, S. Dai, M. Jaroniec, S. Z. Qiao, *J. Am. Chem. Soc.*, **2014**, *136*, 13925.
[5] J. H. Wang, W. Cui, Q. Liu, Z. C. Xing, A. M. Asiri, X. P. Sun, *Adv. Mater.*, **2016**, *28*, 215.
[6] F. Song, X. Hu, *Nature Commun.*, **2014**, *5*, 4477.

[7] X. Xu, F. Song, X. Hu, *Nature Commun.*, **2016**, *7*, 12324.
[8] H. Y. Jin, J. Wang, D. F. Su, Z. Z. Wei, Z. F. Pang, Y. Wang, *J. Am. Chem. Soc.*, **2015**, *137*, 2688.
[9] B. Zhang, X. Zheng, O. Voznyy, R. Comin, M. Bajdich, M. Garcia-Melchor, L. Han, J. Xu, M. Liu, L. Zheng, F. P. Garcia de Arquer, C. T. Dinh, F. Fan, M. Yuan, E. Yassitepe, N. Chen, T. Regier, P. Liu, Y. Li, P. De Luna, A. Janmohamed, H. L. Xin, H. Yang, A. Vojvodic, E. H. Sargent, *Science*, **2016**, *352*, 333.
[10] N. Han, F. P. Zhao, Y. G. Li, *J. Mater. Chem. C.*, **2015**, *3*, 16348.
[11] F. Song, X. Hu, *J. Am. Chem. Soc.*, **2014**, *136*, 16481.
[12] H. Zhou, F. Yu, J. Sun, R. He, S. Chen, C. W. Chu, Z. Ren, *Proc. Natl. Acad. Sci. U. S. A.*, **2017**.
[13] X. Long, J. Li, S. Xiao, K. Yan, Z. Wang, H. Chen, S. Yang, *Angew Chem Int Ed Engl*, **2014**, *53*, 7584.
[14] B. You, Y. J. Sun, *Adv. Energy Mater.*, **2016**, *6*.
[15] M. A. Ghanem, A. M. Al-Mayouf, P. Arunachalam, T. Abiti, *Electrochim. Acta*, **2016**, *207*, 177.
[16] C. G. Morales-Guio, L. Liardet, X. L. Hu, *J. Am. Chem. Soc.*, **2016**, *138*, 8946.
[17] L. Trotochaud, S. L. Young, J. K. Ranney, S. W. Boettcher, *J. Am. Chem. Soc.*, **2014**, *136*, 6744.
[18] Y. P. Liu, X. Y. He, D. Hanlon, A. Harvey, J. N. Coleman, Y. G. Li, *ACS Nano*, **2016**, *10*, 8821.
[19] T. M. Higgins, D. McAteer, J. C. M. Coelho, B. M. Sanchez, Z. Gholamvand, G. Moriarty, N. McEvoy, N. C. Berner, G. S. Duesberg, V. Nicolosi, J. N. Coleman, *ACS Nano*, **2014**, *8*, 9567.
[20] D. McAteer, Z. Gholamvand, N. McEvoy, A. Harvey, E. O'Malley, G. S. Duesberg, J. N. Coleman, *ACS Nano*, **2016**, *10*, 672.
[21] Zheng Ling, Andrew Harvey, David McAteer, Ian J. Godwin, Beata Szydłowska, Aideen Griffin, Victor Vega, Yongchen Song, Andrés Seral-Ascaso, Valeria Nicolosi, J. Coleman, *Adv. Energy Mater.*, **2017**, *in-press*, 1702364.
[22] R. C. Chiu, T. J. Garino, M. J. Cima, *J. Am. Ceram. Soc.*, **1993**, *76*, 2257; K. B. Singh, M. S. Tirumkudulu, *Phys. Rev. Lett.*, **2007**, *98*.
[23] Z. Q. Liu, G. F. Chen, P. L. Zhou, N. Li, Y. Z. Su, *J. Power Sources*, **2016**, *317*, 1.
[24] X. Long, S. Xiao, Z. Wang, X. Zheng, S. Yang, *Chem. Commun.*, **2015**, *51*, 1120.
[25] K. R. Paton, E. Varrla, C. Backes, R. J. Smith, U. Khan, A. O'Neill, C. Boland, M. Lotya, O. M. Istrate, P. King, T. Higgins, S. Barwich, P. May, P. Puczkarski, I. Ahmed, M. Moebius, H. Pettersson, E. Long, J. Coelho, S. E. O'Brien, E. K. McGuire, B. M. Sanchez, G. S. Duesberg, N. McEvoy, T. J. Pennycook, C. Downing, A. Crossley, V. Nicolosi, J. N. Coleman, *Nat. Mater.*, **2014**, *13*, 624.
[26] C. Backes, B. M. Szydłowska, A. Harvey, S. Yuan, V. Vega-Mayoral, B. R. Davies, P.-l. Zhao, D. Hanlon, E. J. G. Santos, M. I. Katsnelson, W. J. Blau, C. Gadermaier, J. N. Coleman, *ACS Nano*, **2016**, *10*, 1589.
[27] A. Harvey, X. He, I. J. Godwin, C. Backes, D. McAteer, N. C. Berner, N. McEvoy, A. Ferguson, A. Shmeliov, M. E. G. Lyons, V. Nicolosi, G. S. Duesberg, J. F. Donegan, J. N. Coleman, *J. Mater. Chem. A*, **2016**, *4*, 11046.
[28] J. H. Huang, J. T. Chen, T. Yao, J. F. He, S. Jiang, Z. H. Sun, Q. H. Liu, W. R. Cheng, F. C. Hu, Y. Jiang, Z. Y. Pan, S. Q. Wei, *Angew. Chem.,Int. Ed.*, **2015**, *54*, 8722.
[29] R. Wang, X. Yan, J. Lang, Z. Zheng, P. Zhang, *J. Mater. Chem. C.*, **2014**, *2*, 12724.
[30] Y. Jiang, X. Li, T. Wang, C. Wang, *Nanoscale*, **2016**, *8*, 9667.
[31] A. J. Esswein, M. J. McMurdo, P. N. Ross, A. T. Bell, T. D. Tilley, *J. Phys. Chem. C*, **2009**, *113*, 15068.
[32] W. Ma, R. Z. Ma, C. X. Wang, J. B. Liang, X. H. Liu, K. C. Zhou, T. Sasaki, *ACS Nano*, **2015**, *9*, 1977.
[33] J. F. Shen, Y. M. He, J. J. Wu, C. T. Gao, K. Keyshar, X. Zhang, Y. C. Yang, M. X. Ye, R. Vajtai, J. Lou, P. M. Ajayan, *Nano Lett.*, **2015**, *15*, 5449.
[34] Y. Hernandez, V. Nicolosi, M. Lotya, F. M. Blighe, Z. Sun, S. De, I. T. McGovern, B. Holland, M. Byrne, Y. K. Gun'Ko, J. J. Boland, P. Niraj, G. Duesberg, S. Krishnamurthy, R. Goodhue, J.

Hutchison, V. Scardaci, A. C. Ferrari, J. N. Coleman, *Nat. Nanotechnol.*, **2008**, *3*, 563; A. Ciesielski, P. Samori, *Chem. Soc. Rev.*, **2014**, *43*, 381.
[35] C. Y. Zhi, Y. Bando, C. C. Tang, H. Kuwahara, D. Golberg, *Adv. Mater.*, **2009**, *21*, 2889.
[36] J. N. Coleman, M. Lotya, A. O'Neill, S. D. Bergin, P. J. King, U. Khan, K. Young, A. Gaucher, S. De, R. J. Smith, I. V. Shvets, S. K. Arora, G. Stanton, H. Y. Kim, K. Lee, G. T. Kim, G. S. Duesberg, T. Hallam, J. J. Boland, J. J. Wang, J. F. Donegan, J. C. Grunlan, G. Moriarty, A. Shmeliov, R. J. Nicholls, J. M. Perkins, E. M. Grieveson, K. Theuwissen, D. W. McComb, P. D. Nellist, V. Nicolosi, *Science*, **2011**, *331*, 568; K. G. Zhou, N. N. Mao, H. X. Wang, Y. Peng, H. L. Zhang, *Angew. Chem.,Int. Ed.*, **2011**, *50*, 10839.
[37] S. Mandeep, G. Enrico Della, A. Taimur, W. Sumeet, R. Rajesh, E. Joel van, M. Edwin, B. Vipul, *2D Materials*, **2017**, *4*, 025110.
[38] D. Hanlon, C. Backes, E. Doherty, C. S. Cucinotta, N. C. Berner, C. Boland, K. Lee, A. Harvey, P. Lynch, Z. Gholamvand, S. F. Zhang, K. P. Wang, G. Moynihan, A. Pokle, Q. M. Ramasse, N. McEvoy, W. J. Blau, J. Wang, G. Abellan, F. Hauke, A. Hirsch, S. Sanvito, D. D. O'Regan, G. S. Duesberg, V. Nicolosi, J. N. Coleman, *Nature Commun.*, **2015**, *6*; J. R. Brent, N. Savjani, E. A. Lewis, S. J. Haigh, D. J. Lewis, P. O'Brien, *Chem. Commun.*, **2014**, *50*, 13338.
[39] A. J. Molina-Mendoza, E. Giovanelli, W. S. Paz, M. A. Nino, J. O. Island, C. Evangeli, L. Aballe, M. Foerster, H. S. J. van der Zant, G. Rubio-Bollinger, N. Agrait, J. J. Palacios, E. M. Perez, A. Castellanos-Gomez, *Nature Commun.*, **2017**, *8*.
[40] H. Andrew, B. B. John, G. Ian, G. K. Adam, M. S. Beata, M. Ghulam, T. Andrew, J. L. David, O. B. Paul, N. C. Jonathan, *2D Materials*, **2017**, *4*, 025054.
[41] M. Lotya, Y. Hernandez, P. J. King, R. J. Smith, V. Nicolosi, L. S. Karlsson, F. M. Blighe, S. De, Z. Wang, I. T. McGovern, G. S. Duesberg, J. N. Coleman, *J. Am. Chem. Soc.*, **2009**, *131*, 3611; R. J. Smith, P. J. King, M. Lotya, C. Wirtz, U. Khan, S. De, A. O'Neill, G. S. Duesberg, J. C. Grunlan, G. Moriarty, J. Chen, J. Z. Wang, A. I. Minett, V. Nicolosi, J. N. Coleman, *Adv. Mater.*, **2011**, *23*, 3944.
[42] Z. P. Liu, R. Z. Ma, M. Osada, K. Takada, T. Sasaki, *J. Am. Chem. Soc.*, **2005**, *127*, 13869.
[43] A. G. Kelly, T. Hallam, C. Backes, A. Harvey, A. S. Esmaeily, I. Godwin, J. Coelho, V. Nicolosi, J. Lauth, A. Kulkarni, S. Kinge, L. D. A. Siebbeles, G. S. Duesberg, J. N. Coleman, *Science*, **2017**, *356*, 69.
[44] A. Harvey, C. Backes, Z. Gholamvand, D. Hanlon, D. McAteer, H. C. Nerl, E. McGuire, A. Seral-Ascaso, Q. M. Ramasse, N. McEvoy, S. Winters, N. C. Berner, D. McCloskey, J. F. Donegan, G. S. Duesberg, V. Nicolosi, J. N. Coleman, *Chem. Mater.*, **2015**, *27*, 3483.
[45] Y. C. Liu, J. A. Koza, J. A. Switzer, *Electrochim. Acta*, **2014**, *140*, 359.
[46] T. F. Jaramillo, K. P. Jorgensen, J. Bonde, J. H. Nielsen, S. Horch, I. Chorkendorff, *Science*, **2007**, *317*, 100; B. Hinnemann, P. G. Moses, J. Bonde, K. P. Jorgensen, J. H. Nielsen, S. Horch, I. Chorkendorff, J. K. Norskov, *J. Am. Chem. Soc.*, **2005**, *127*, 5308; J. Benson, M. X. Li, S. B. Wang, P. Wang, P. Papakonstantinou, *ACS Appl. Mater. Interfaces*, **2015**, *7*, 14113; W. Hirunpinyopas, A. N. J. Rodgers, S. D. Worrall, M. A. Bissett, R. A. W. Dryfe, *ChemNanoMat*, **2017**, *3*, 428.
[47] Z. Gholamvand, D. McAteer, A. Harvey, C. Backes, J. N. Coleman, *Chem. Mater.*, **2016**, *28*, 2641.
[48] J. Chen, A. Selloni, *J. Phys. Chem. C*, **2013**, *117*, 20002.
[49] L. Qian, Z. Y. Lu, T. H. Xu, X. C. Wu, Y. Tian, Y. P. Li, Z. Y. Huo, X. M. Sun, X. Duan, *Adv. Energy Mater.*, **2015**, *5*.
[50] A. S. Batchellor, S. W. Boettcher, *ACS Catal.*, **2015**, *5*, 6680.
[51] M. Gong, Y. G. Li, H. L. Wang, Y. Y. Liang, J. Z. Wu, J. G. Zhou, J. Wang, T. Regier, F. Wei, H. J. Dai, *J. Am. Chem. Soc.*, **2013**, *135*, 8452.
[52] Y. P. Liu, X. Y. He, D. Hanlon, A. Harvey, U. Khan, Y. G. Li, J. N. Coleman, *ACS Nano*, **2016**, *10*, 5980.
[53] F. Malara, S. Corallo, E. Rotunno, L. Lazzarini, E. Piperopoulos, C. Milone, A. Naldoni, *ACS Catal.*, **2017**.
[54] G. Lota, K. Fic, E. Frackowiak, *Energy Environ. Sci.*, **2011**, *4*, 1592.
[55] G. Cunningham, M. Lotya, N. McEvoy, G. S. Duesberg, P. van der Schoot, J. N. Coleman, *Nanoscale*, **2012**, *4*, 6260; D. A. Stauffer, A., *Introduction to Percolation Theory*, Taylor & Francis, London 1985.

[56] C. C. L. McCrory, S. Jung, J. C. Peters, T. F. Jaramillo, *J. Am. Chem. Soc.*, **2013**, *135*, 16977; J. M. Barforoush, D. T. Jantz, T. E. Seuferling, K. R. Song, L. C. Cummings, K. C. Leonard, *J. Mater. Chem. C.*, **2017**.
[57] J. Suntivich, K. J. May, H. A. Gasteiger, J. B. Goodenough, Y. Shao-Horn, *Science*, **2011**, *334*, 1383; R. L. Doyle, I. J. Godwin, M. P. Brandon, M. E. G. Lyons, *Phys. Chem. Chem. Phys.*, **2013**, *15*, 13737.
[58] V. I. Birss, A. Damjanovic, *J. Electrochem. Soc.*, **1987**, *134*, 113; R. L. Doyle, M. E. G. Lyons, *Phys. Chem. Chem. Phys.*, **2013**, *15*, 5224; J. O. Bockris, T. Otagawa, *J. Phys. Chem.*, **1983**, *87*, 2960.
[59] T. Reier, M. Oezaslan, P. Strasser, *ACS Catal.*, **2012**, *2*, 1765.
[60] M. S. Burke, L. J. Enman, A. S. Batchellor, S. Zou, S. W. Boettcher, *Chem. Mater.*, **2015**, *27*, 7549.
[61] M. H. Miles, G. Kissel, P. W. T. Lu, S. Srinivasan, *J. Electrochem. Soc.*, **1976**, *123*, 332.
[62] S. Chen, J. Duan, M. Jaroniec, S.-Z. Qiao, *Adv. Mater.*, **2014**, *26*, 2925; S. Chen, S. Z. Qiao, *ACS Nano*, **2013**, *7*, 10190.